Energy Engineering

Tech Science Press

Doi:10.32604/ee.2025.074054

ARTICLE

Research on MPPT Control and Grid-Connected and Off-Grid Operation Control Strategy of Photovoltaic-Storage Microgrid Based on PSO Algorithm

Tao Wang[1], Ze Feng[1,*], Jinghao Ma[2], Shenhui Chen[2], Jihui Zhang[2] and Tong Wang[2]

[1]Mechanical Engineering, College of Mechanical and Equipment Engineering, New Campus, Hebei University of Engineering, Handan, 056038, China

[2]College of Mechanical and Equipment Engineering, Hebei University of Engineering, Handan, 056038, China

*Corresponding Author: Ze Feng. Email: 15062940565@163.com

Received: 30 September 2025; Accepted: 20 November 2025; Published: 18 June 2026

ABSTRACT: This paper develops an MPPT control strategy utilizing the particle swarm optimization (PSO) algorithm to enhance the tracking accuracy of photovoltaic arrays under complex operating conditions and to mitigate the transient effects on energy storage batteries during grid-connected and off-grid transitions. Initially, the operational principle of the three-phase voltage source PWM converter and the bidirectional DC/DC converter within solar power generation and energy storage systems is carefully examined, leading to the establishment of the appropriate mathematical model. Secondly, a voltage and current double closed-loop control structure utilizing feedforward decoupling is devised to meet the cooperative control requirements of multi-energy units in a microgrid. The integration of constant power (PQ) control, virtual synchronous motor (VSG) management, and constant current and voltage charging and discharging strategies facilitate the seamless interaction of energy storage systems and the smooth transition between grid-connected and off-grid states. The integration of multiple control links enhances MPPT tracking accuracy and dynamic response speed, effectively mitigating current and voltage fluctuations during the switching process, thereby significantly improving the system's transient performance and operational stability in the microgrid. Finally, the simulation model is constructed using MATLAB/Simulink to validate the control approach presented in this paper. The simulation findings indicate that the control approach exhibits commendable dynamic performance, stability, and engineering feasibility in complicated operational settings.

KEYWORDS: Photovoltaic energy storage microgrid; PSO algorithm; voltage and current double closed-loop control; PQ control; VSG control

1 Introduction

Amid the escalation of the global energy crisis and the growing awareness of environmental protection, solar energy, recognized as an eco-friendly and renewable resource, has gained prominence. It is frequently developed and utilized as distributed power sources to establish dependable and stable distributed power generation technology [1–3]. Photovoltaic cells are the primary medium for transforming solar energy into electrical energy. Its utilization rate is intrinsically linked to maximum power point tracking. Adopting a judicious MPPT control approach is of paramount importance. The prevalent techniques include the incremental conductance method (INC), perturbation and observation method (P&O), fuzzy control method (Fuzzy), and several enhanced algorithms [4–8]. Reference [9] proposed an artificial rabbit optimization algorithm (ARO) to determine the maximum size of the battery energy storage system in the microgrid to minimize operating costs. Compared with other algorithms, it shows effectiveness and robustness. Reference [10]

presented a MPPT methodology that combines the cuckoo algorithm with the conductance increment technique. The cuckoo algorithm is first utilized for global optimization, subsequently succeeded by the conduct increment method for precise localization.

The variability of solar power generation, influenced by temperature and illumination, necessitates the incorporation of an energy storage system to stabilize and establish a microgrid system [11,12]. The microgrid can function in both grid-connected mode with the larger power grid via a common connection point and can swiftly disconnect to operate in off-grid (island) mode during a fault. In this mode, it independently supplies power to local loads while maintaining voltage and frequency stability through the converter's control strategy [13]. The prevalent control modes of microgrids include master-slave control and peer-to-peer control. Photovoltaic energy storage microgrids typically employ master-slave control systems [14]. The prevalent control strategies employed in the converter encompass PQ control, V/f control, droop control, and VSG control, among others [15–18]. Reference [19] advocated employing a PQ + PQ control approach for grid-connected operation and a V/f + PQ comprehensive control method for off-grid operation to achieve seamless transition from grid-connected to off-grid mode in optical storage microgrids, therefore enhancing stability. Reference [20] indicated that to guarantee stable and efficient synchronization of the microgrid cluster during the transition between island mode and grid-connected mode, while minimizing frequency deviation and enhancing power sharing, a seamless synchronization control utilizing the differential evolution algorithm was devised to address the deficiency of a robust, rapid, and quantifiable synchronization method in microgrid clusters employing hybrid inverters. Reference [21] addresses the power balance issue of the microgrid during off-grid operation following a power grid failure, examines prevalent operational modes, and investigates the seamless transition method between maximum power point tracking and stable voltage control processes of the photovoltaic array. Simultaneously, adaptive droop control is implemented for the energy storage unit to prevent the risk of overcharging or overdischarging. Reference [22] introduced a multi-parameter cooperative adaptive control strategy derived from the conventional VSG control strategy, which significantly mitigated substantial output fluctuations and inadequate response performance during the grid-connected transient process; however, it overlooked the examination of the converter control effect in the off-grid mode of the microgrid. Reference [23] introduced the concept of hybrid energy storage and established the power stratification point for the transition of batteries and supercapacitors to operational mode, employing droop control of the acceleration factor based on state of charge (SOC) data; however, its primary emphasis is on the investigation of micro-grid control strategies that incorporate hybrid energy storage.

This study provides a comprehensive overview of the structure of photovoltaic energy storage microgrids and presents enhancements and innovations to the conventional photovoltaic maximum power point tracking algorithm. The MPPT control strategy employs a particle swarm optimization algorithm to enhance tracking precision and response velocity. A voltage and current double closed-loop control system utilizing feedforward decoupling is proposed to augment the anti-interference capability of the system. Two control mechanisms of the energy storage system converter are examined: constant power control and VSG control. In grid-connected operation mode, the system must maintain a constant power connection to the grid to mitigate the effects of fluctuations in photovoltaic output power on the voltage at the common coupling point (PCC). Consequently, a control method based on PCC voltage has been developed for the energy storage battery. The energy storage battery absorbs and discharges varying powers to sustain the stability of the bus voltage. Simultaneously, a bidirectional DC/DC converter is employed to extend battery lifespan, and a constant current constant voltage charging and discharging control technique is formulated. Upon transitioning from grid-connected mode to off-grid mode, the control mode concurrently shifts to VSG control, thereby markedly mitigating transient effects on the system during the control strategy transition. This effectively preserves the stability of the internal voltage and frequency of the microgrid, facilitating

stable operation in off-grid mode. The MATLAB/Simulink simulation platform is employed to construct the photovoltaic energy storage system, and a parallel/off-grid simulation analysis is conducted to validate the stability and feasibility of the system control.

The design framework of this article will be delineated in the subsequent chapters: The second chapter introduces the MPPT control technique with the particle swarm optimization algorithm. The third portion establishes the mathematical model of the solar energy storage microgrid structure, together with the three-phase voltage source PWM converter and the bidirectional DC/DC converter. The fourth section examines the control strategies of solar inverters, bidirectional DC/DC converters, and energy storage converters in both grid-connected and off-grid scenarios. Ultimately, in the fifth portion, the simulation validation is conducted on the MATLAB/Simulink platform, which substantiates the viability of the system's control strategy coordination.

2 Photovoltaic Maximum Power Point Tracking Principle and Control Strategy

2.1 Photovoltaic Maximum Power Point Tracking Principle

The photovoltaic cell produces free electrons and holes via the photovoltaic effect of the semiconductor PN junction, converting light energy into electrical energy [24]. The output power characteristic curve is a single peak function, with the maximum power point representing the extreme value. To optimize the performance of solar cells and enhance the conversion of light energy into electrical energy, it is essential to use control strategies that adapt the photovoltaic system in real time, ensuring sustained operational output at peak power points.

The infinitesimal technique posits that the characteristic curve of photovoltaic cells can be considered a linear system over a brief duration. As seen in Fig. 1, U_0 represents the solar voltage source, R_0 denotes the output impedance of the photovoltaic cell, and R_1 signifies the load impedance.

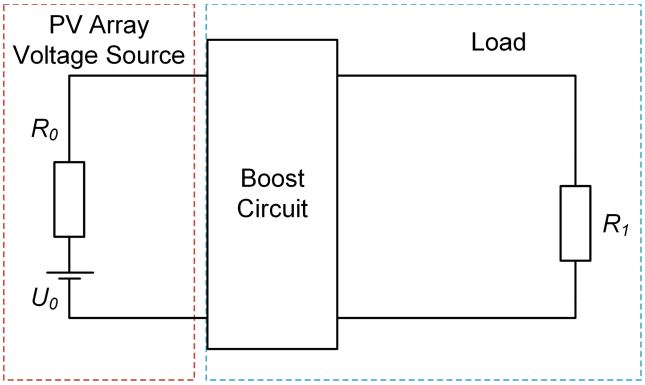

Figure 1: Photovoltaic source impedance circuit

The power P of the load resistor is defined as:

$$P = \left(\frac{U_0}{R_0 + R_1}\right) \cdot R_1 \tag{1}$$

The derivation of Eq. (1) can be attained:

$$\frac{dP}{dR_1} = {U_0}^2 \cdot \frac{R_0 - R_1}{(R_0 + R_1)^3} \tag{2}$$

To achieve $dP/dR_1 = 0$, If and only if $R_0 = R_1$, At this time, $P = P_{max}$, and the power production is at its maximum capacity. The MPPT control process of photovoltaic power generation system is the process of matching the output impedance and load impedance.

2.2 MPPT Control Strategy Based on Particle Swarm Optimization Algorithm

The particle swarm optimization algorithm is a numerical optimization technique grounded in swarm intelligence. The concept is inspired by the collective behavior of birds or fish, particularly their cooperative actions while foraging. The particle swarm optimization approach is applicable to both multi-peak convex optimization issues and single-peak problems. The program delineates a collection of N particles traversing at a specific velocity within the D-dimensional search space. Each 'particle' in the exploration space signifies a potential solution within the solution space. Every particle possesses a fitness value calculated by the objective function. A solitary particle acquires the ideal solution by iteratively refining the two parameters of position and velocity, thereafter, comparing them to ultimately identify the global optimum position.

In the context of maximizing value, a higher objective function value correlates with an improved fitness value In the particle swarm optimization process, the individual ideal position $P_i^{(t)}$ for particle i, after t repetitions, is defined by Eq. (3):

$$P_i{}^{(t)} = \begin{cases} x_i{}^{(t)} & f\left[x_i{}^{(t)}\right] > f\left[p_i{}^{(t-1)}\right] \\ p_i{}^{(t-1)} & f\left[x_i{}^{(t)}\right] \le f\left[p_i{}^{(t-1)}\right] \end{cases} \tag{3}$$

The optimal location $G^{(t)}$ of the population is ascertained by the maximum value of the set of all particles $P_i{}^{(t)}$, and this optimal position is defined by Formulas (4) and (5):

$$g = \arg\max_{1 \le i \le N} \left\{ f\left[P_i{}^{(t)}\right] \right\} \tag{4}$$

$$G^{(t)} = P_g{}^{(t)} \tag{5}$$

According to the definition, the formula for updating the position and velocity of an individual particle in the PSO algorithm is:

$$x_i{}^{(t+1)} = x_i{}^{(t)} + v_i{}^{(t+1)} \tag{6}$$

$$v_i{}^{(t+1)} = \omega \cdot v_i{}^{(t)} + c_1 r_1 \cdot \left(P_i{}^{(t)} - x_i{}^{(t)}\right) + c_2 r_2 \cdot \left(G^{(t)} - x_i{}^{(t)}\right) \tag{7}$$

In the formula previously mentioned, $x_i{}^{(t)}$ and $v_i{}^{(t)}$ represent the position and velocity of the i particle at the t iteration; $P_i{}^{(t)}$ denotes the individual experience optimal position of the first particle; $G^{(t)}$ represents the optimal place of population experience; t is the number of iterations; ω represents the inertia weight, and the magnitude of ω significantly impacts both local and global search capabilities; c_1 denotes the acceleration coefficient of the particle moving towards the individual's optimal position; c_2 signifies the acceleration coefficient of the particle advancing towards the global optimal position; r_1, r_2 are random numbers inside the interval $[0, 1]$.

Certain parameters in the PSO algorithm can influence its performance and perhaps compromise the correctness of the answer. A bigger population size increases the number of particles, enhancing global search capabilities, but incurs higher computing costs. A reduced population size results in fewer particles, accelerates convergence speed, but increases the likelihood of succumbing to local optima. To mitigate the deficiencies of various elements, the particle count N in the PSO algorithm presented in this paper is 30; To

attain a relative equilibrium between exploration and development, ω is established at 0.5; Assign $c_1 = c_2 = 2$; accord equal consideration to individual experience and collective experience. The direction of the speed update can be calculated from Formula (7), as illustrated in Fig. 2:

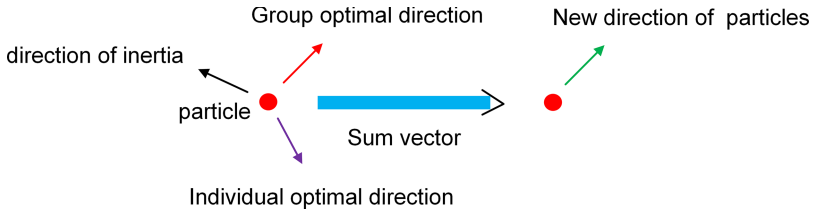

Figure 2: Speed direction update diagram

Fig. 3 illustrates the flowchart of the PSO algorithm:

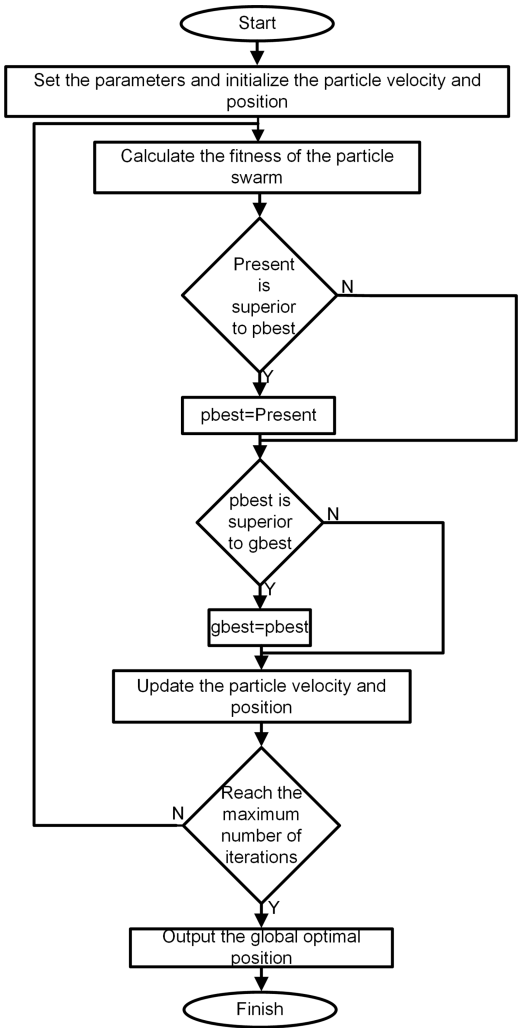

Figure 3: Flow chart of PSO algorithm

The crux of the maximum power point tracking issue in solar power generating systems is the optimization of the photovoltaic array's output power. Consequently, the PSO_MPPT algorithm is applicable

to solar MPPT. The position x_i of the particle denotes the reference value of the output voltage of the photovoltaic array, while the velocity v_i of the particle signifies the adjustment step and direction of the output voltage. To assess the efficacy of the algorithm, the circuit diagram of the photovoltaic power generating system regulated by PSO_MPPT, as depicted in Fig. 4, is utilized. The system comprises four components: solar array, Boost circuit, PSO algorithm module, and load.

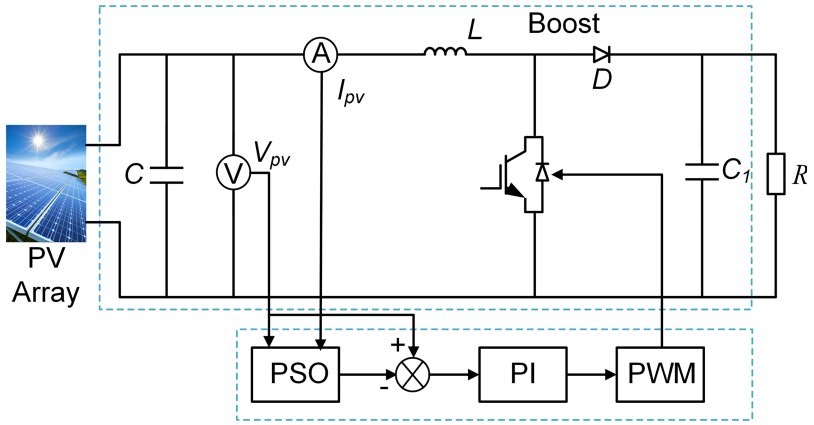

Figure 4: Circuit diagram of photovoltaic power generation system based on PSO_MPPT control

When solar irradiance and temperature are specified, the theory of maximum power point tracking dictates that the photovoltaic array delivers maximum power when the output impedance is equivalently matched to the load impedance. A simulation model in MATLAB/Simulink employing the particle swarm optimization approach for MPPT control has been developed. As illustrated in Fig. 5. The Function module encapsulates the prepared particle swarm optimization method within a subsystem. The system utilizes the output voltage and current of the photovoltaic cell as inputs, which subsequently regulate the duty cycle of the DC chopper switch to manage the pulse. The output impedance is adjusted to match the internal resistance by modifying the duty cycle, thereby enabling the photovoltaic cell to operate at its maximum power point.

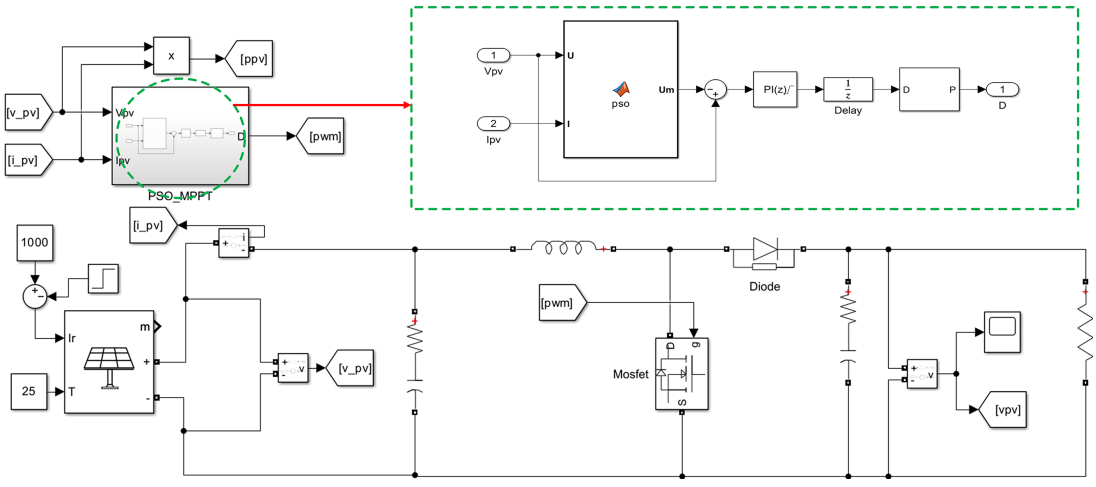

Figure 5: Simulation model of photovoltaic power generation based on PSO_MPPT control

3 The Establishment of Topology and Mathematical Model of Photovoltaic Energy Storage Microgrid System

3.1 Optical Storage Micro-Grid Structure

The configuration of the optical storage microgrid presented in this paper is illustrated in Fig. 6. The photovoltaic system functions as the primary power source for the load. The energy storage module regulates charge and discharge via the bidirectional Buck-Boost circuit, interfaces with the critical load through the bidirectional AC/DC converter and ultimately integrates into the distribution network at the Point of Common Coupling. The photovoltaic power generating system employs MPPT control utilizing a particle swarm optimization technique to maximize power output, while the photovoltaic inverter implements double closed-loop control with feedforward decoupling. The energy storage converter employs PQ control in grid-connected mode to achieve a stable power connection and maintain the system's power quality. In off-grid mode, the energy storage converter is transitioned to VSG management to maintain system voltage and frequency stability, hence facilitating the reliable operation of the microgrid.

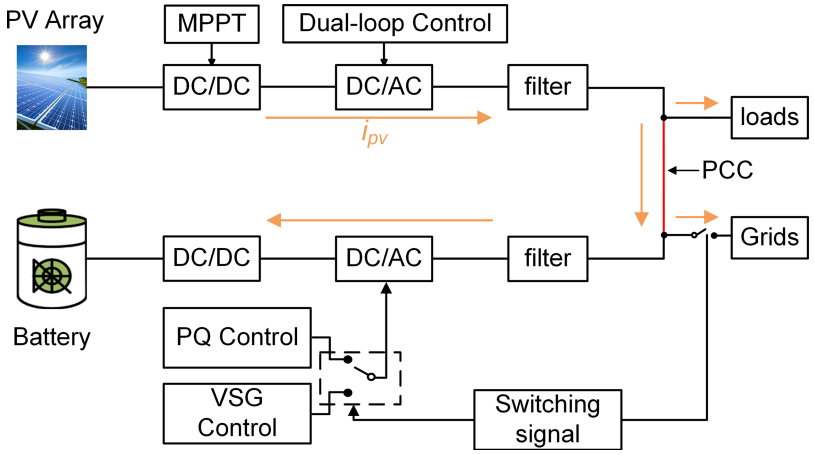

Figure 6: Structure diagram of photovoltaic energy storage microgrid system

3.2 Topology and Mathematical Model of Voltage Source PWM Converter

The three-phase voltage source PWM inverter comprises six power switching components. The AC side employs a three-phase symmetrical connection method, directly interfacing with the three-phase lines of the power grid. The entire system demonstrates robust coupling properties and nonlinearity. The six switch tubes operate in a complimentary conduction mode of the upper and lower half bridges, with the switch tube signals created by space vector pulse width modulation technology to achieve the desired control effect. Fig. 7 illustrates the configuration of the primary circuit of the photovoltaic energy storage system.

In Fig. 7, S_1~S_6 are the power switch transistors of the three-phase PWM converter utilized in the photovoltaic system. S_{15} serves as the power switch tube for the Boost circuit, while U_{dc} represents the DC bus voltage of the photovoltaic system. S_7~S_{12} are the PWM converter power switch tubes of the energy storage system. S_{13} and S_{14} function as bidirectional DC/DC power switches, while U^*_{dc} represents the DC bus voltage of the energy storage system.L and L_2 are filter inductors, and R, R_2 are parasitic resistors.

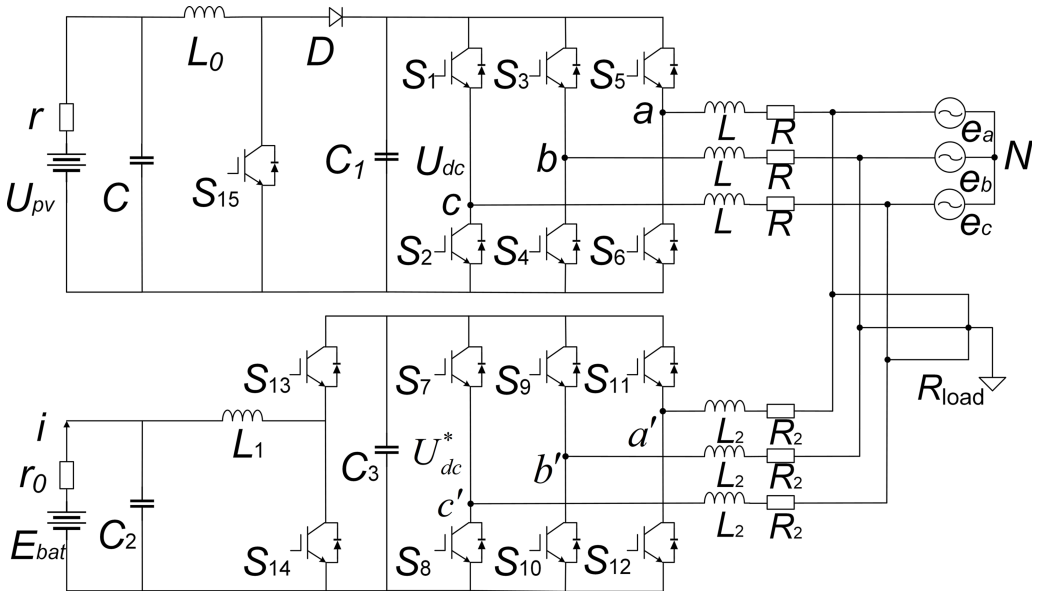

Figure 7: Main circuit topology

Fig. 7 demonstrates that the mathematical model of the three-phase stationary coordinate system is established using Kirchhoff's theorem:

$$L\frac{d}{dt}\begin{bmatrix} i_a \\ i_b \\ i_c \end{bmatrix} = \begin{bmatrix} e_a \\ e_b \\ e_c \end{bmatrix} - R\begin{bmatrix} i_a \\ i_b \\ i_c \end{bmatrix} - \begin{bmatrix} u_a \\ u_b \\ u_c \end{bmatrix} \tag{8}$$

In Formula (8), i_a, i_b, i_c represent the phase currents a, b, c at the grid side; e_a, e_b, e_c denote the grid phase voltages a, b, c; u_a, u_b, u_c signify the phase voltages a, b, c between the converter's input terminal and the neutral point N; L indicates the network side filter inductance; R refers to parasitic resistance.

In the three-phase stationary coordinate system, the three-phase variables are interdependent and vary throughout time. The analysis of one phase's behavior is frequently influenced by the other two phases. To address this issue and enhance the efficiency and stability of the system control, the three-phase stationary coordinate system ($a-b-c$ coordinate system) is converted into a two-phase stationary coordinate system ($\alpha-\beta$ coordinate system) via Clarke transformation, followed by the transformation of the two-phase stationary coordinate system into a two-phase rotating coordinate system ($d-q$ coordinate system) through Park transformation. The previously mentioned transformation enables the conversion of the original AC quantity into a DC quantity, significantly simplifying the design of the control strategy and enhancing the system's dynamic response performance.

The link between the three-phase stationary coordinate system and the two-phase stationary coordinate system is established through Clarke transformation:

$$\begin{bmatrix} x_\alpha \\ x_\beta \end{bmatrix} = \frac{2}{3}\begin{bmatrix} 1 & -\frac{1}{2} & -\frac{1}{2} \\ 0 & \frac{\sqrt{3}}{2} & -\frac{\sqrt{3}}{2} \end{bmatrix}\begin{bmatrix} x_a \\ x_b \\ x_c \end{bmatrix} \tag{9}$$

In Eq. (9), the variables x_α and x_β denote the α and β axis variables in the $\alpha - \beta$ coordinate system, whereas x_a, x_b, and x_c signify the a, b, and c phase variables in the $a - b - c$ coordinate system.

The mathematical model of the $\alpha - \beta$ coordinate system can be derived by integrating Formula (8) with Formula (9):

$$L\frac{d}{dt}\begin{bmatrix} i_\alpha \\ i_\beta \end{bmatrix} = \begin{bmatrix} e_\alpha \\ e_\beta \end{bmatrix} - R\begin{bmatrix} i_\alpha \\ i_\beta \end{bmatrix} - \begin{bmatrix} u_\alpha \\ u_\beta \end{bmatrix} \tag{10}$$

In Formula (10), i_α and i_β denote the current components in the $\alpha - \beta$ coordinate system derived from the Clarke transformation of three-phase AC current; e_α and e_β signify the voltage components obtained from the transformation of three-phase AC voltage; u_α and u_β represent the voltage components of the converter's AC side voltage post-conversion.

The correlation between Eq. (10) and the $d - q$ coordinate system via Park transformation is:

$$\begin{bmatrix} x_d \\ x_q \end{bmatrix} = \begin{bmatrix} \cos\omega t & \sin\omega t \\ -\sin\omega t & \cos\omega t \end{bmatrix}\begin{bmatrix} x_\alpha \\ x_\beta \end{bmatrix} \tag{11}$$

In Eq. (11), the physical quantities x_d and x_q denote the d and q axis components in the $d - q$ coordinate system; ω represents the angular velocity of rotation.

The mathematical model of the $d - q$ coordinate system can be derived by integrating Formula (10) with Formula (11).

$$L\frac{d}{dt}\begin{bmatrix} i_d \\ i_q \end{bmatrix} = \begin{bmatrix} e_d \\ e_q \end{bmatrix} - R\begin{bmatrix} i_d \\ i_q \end{bmatrix} - \begin{bmatrix} u_d \\ u_q \end{bmatrix} + \omega L\begin{bmatrix} i_q \\ -i_d \end{bmatrix} \tag{12}$$

In Eq. (12), i_d and i_q represent the components of the three-phase AC current in the $d - q$ coordinate system after transformation; e_d and e_q signify the voltage component in the $d - q$ coordinate system; u_d and u_q indicate the converter AC side voltage component in the $d - q$ coordinate system.

The Laplace transform is used to Eq. (12), resulting in the mathematical model in the corresponding frequency domain as follows:

$$\begin{cases} sLi_d = u_d - e_d - Ri_d + \omega Li_q \\ sLi_q = u_q - e_d - Ri_q + \omega Li_d \end{cases} \tag{13}$$

In type (13), s is the Laplace complex variable.

3.3 The Mathematical Model of Bidirectional DC/DC Converter Is Established

A bidirectional DC/DC converter is a power conversion apparatus capable of facilitating bidirectional energy transfer. The prevalent architecture is the Buck/Boost circuit. Its primary role is to regulate the output duty cycle by modifying the space vector pulse modulation signal that influences the power switch transistor. The boost and buck are successfully implemented, fulfilling the objectives of charging and draining the energy storage battery. Fig. 8 is the circuit structure diagram:

The energy storage battery is currently in discharge mode. The bidirectional DC/DC converter functions as a boost chopper circuit to elevate the lower voltage of the battery to the higher voltage demanded by the grid or load. At its interior, the inductor stores and subsequently releases energy, thereby increasing the

voltage through the high-speed switching of the switch tube. Currently, S_{14} is turned off and the freewheeling diode D_{13} is turned on. According to Kirchhoff's theorem:

$$L_1 \frac{di}{dt} + r_0 i + E_{bat} = 0 \tag{14}$$

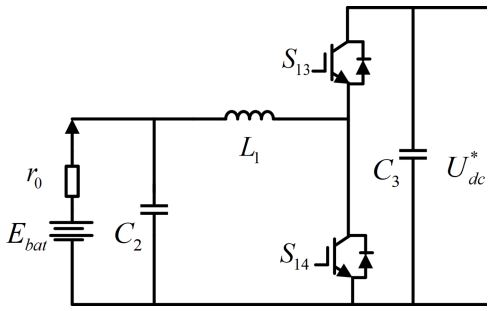

Figure 8: Bidirectional DC/DC converter circuit structure diagram

In type (14), i is expressed as discharge current; E_{bat} represents the electromotive force of the energy storage battery; r_0 corresponds to the internal resistance of the battery, and L_1 signifies the inductance of the DC side.

Eq. (14) is resolved using three elements to determine i. When the power diode S_{13} is deactivated, the current i attains its maximum value I_2.

$$\begin{cases} i = I_1 e^{-\frac{t}{\tau}} + \dfrac{E_{bat}}{r_0}\left(1 - e^{-\frac{t}{\tau}}\right) \\ I_2 = I_1 e^{-\frac{t_{on}}{\tau}} + \dfrac{E_{bat}}{r_0}\left(1 - e^{-\frac{t_{on}}{\tau}}\right) \end{cases} \tag{15}$$

In Formula (15), $\tau = L_0/R_0$ is defined as a time constant; I_1 represents the starting current value when D_{13} is activated, and t_{on} denotes the switch tube's on-time.

Upon deactivation of the power diode S_{13}, the D_{14} is engaged to establish a transfer pathway. The first maximum current value during the transient phase is designated as I_2, while L_1 discharges energy.

$$L_1 \frac{di}{dt} + r_0 i + E_{bat} = U^*{}_{dc} \tag{16}$$

In Eq. (16), $U^*{}_{dc}$ is the DC bus voltage of the energy storage system.

Eq. (16) is resolved using three elements to determine i. When D_{14} is deactivated, the current i equals the original current value I_1 at the moment S_{13} is activated.

$$\begin{cases} i = I_2 e^{-\frac{t_{off}}{\tau}} + \dfrac{U^*{}_{dc} - E_{bat}}{r_0}\left(1 - e^{-\frac{t_{off}}{\tau}}\right) \\ I_1 = I_2 e^{-\frac{t_{off}}{\tau}} + \dfrac{U^*{}_{dc} - E_{bat}}{r_0}\left(1 - e^{-\frac{t_{off}}{\tau}}\right) \end{cases} \tag{17}$$

In Eq. (17), t_{off} indicates the switch's turn-off time.

Combining Eq. (15) with Eq. (17), we can get:

$$U^*_{dc} = \frac{t_{on} + t_{off}}{t_{off}} E_{bat} = \frac{T}{t_{off}} E_{bat} = \frac{1}{1-\alpha} E_{bat} \tag{18}$$

When $T/t_{off} \geq 1$, the circuit is in the boost state, and the energy storage battery discharges.

The energy storage battery is in charging mode. To safely and reliably decrease the elevated grid voltage to a lower voltage suitable for the battery, the bidirectional DC/DC converter functions as a step-down chopper circuit. The calculation steps are the same as above. The process is no longer described here. The final formula is:

$$U^*_{dc} = \frac{t_{on}}{t_{on} + t_{off}} E_{bat} = \frac{t_{on}}{T} E_{bat} = \alpha E_{bat} \tag{19}$$

When $T/t_{off} < 1$, the circuit is in a step-down state, and the energy storage battery is charged.

3.4 Output Power Analysis

During normal circuit operation, four power units are produced. The photovoltaic system's output power is denoted as P_{pv}, the energy storage system's output power as P_{bat}, the load's power as P_{load}, and the grid's power as P_{grid}.

3.4.1 Grid-Connected Operation of Photovoltaic Energy Storage System

$$P_{pv} + P_{bat} - P_{load} - P_{grid} = 0 \tag{20}$$

In the photovoltaic system, the photovoltaic component consistently generates power in a positive state. In the energy storage system, the energy storage battery exhibits a positive condition during discharge and a negative state during charging. The load consistently consumes power, maintaining a negative state, while the photovoltaic output exceeds the load consumption.

The Formula (20) elucidates the link among the four variables and facilitates the assessment of the energy storage battery's operational status:

1. When $P_{pv} > P_{grid} + P_{load}$, then $P_{bat} < 0$, $P_{pv} = P_{grid} + P_{load} - P_{bat}$, at this time, the battery is in charge state, the state of charge increases, and the bidirectional DC/DC converter is in step-down state.

2. When $P_{pv} < P_{grid} + P_{load}$, then $P_{bat} > 0$, $P_{pv} + P_{bat} = P_{load} + P_{grid}$, the battery is in the discharge state, the state of charge is reduced, and the bidirectional DC/DC converter is in the boost state.

3. When $P_{pv} = P_{grid} + P_{load}$, $P_{bat} = 0$, the state of charge of the battery remains unchanged, and there is no energy flow.

3.4.2 Photovoltaic Energy Storage System Off-Grid Operation

$$P_{pv} + P_{bat} - P_{load} = 0 \tag{21}$$

The Formula (21) elucidates the link among the three variables and enables the assessment of the energy storage battery's operational state:

1. When $P_{pv} > P_{load}$, then $P_{bat} < 0$, $P_{pv} = P_{load} + P_{bat}$, currently, the battery absorbs excess power, is in a state of charge, the state of charge increases, and the bidirectional DC/DC converter is in a state of buck.

2. When $P_{pv} < P_{load}$, then $P_{bat} > 0$, $P_{pv} + P_{bat} = P_{load}$, the battery releases power, is in a discharge state, the state of charge is reduced, and the bidirectional DC/DC converter is in a boost state.

3. When $P_{pv} = P_{load}$, $P_{bat} = 0$, the battery has no energy flow, and the state of charge remains stable.

4 Research on Grid-Connected and Off-Grid Control Strategy of Photovoltaic Energy Storage System

4.1 Control Strategy of Voltage Source PWM Converter for Photovoltaic System

The three-phase voltage source PWM converter in a photovoltaic system has a dual closed-loop control strategy consisting of an outer voltage loop and an inner current loop. The voltage outer loop output dictates the input for the current inner loop. The synchronous phase locking technique is employed to guarantee frequency synchronization and phase alignment between the inverter and the grid. The space vector pulse technology is employed to produce the signals for six power switches. As illustrated in Fig. 9:

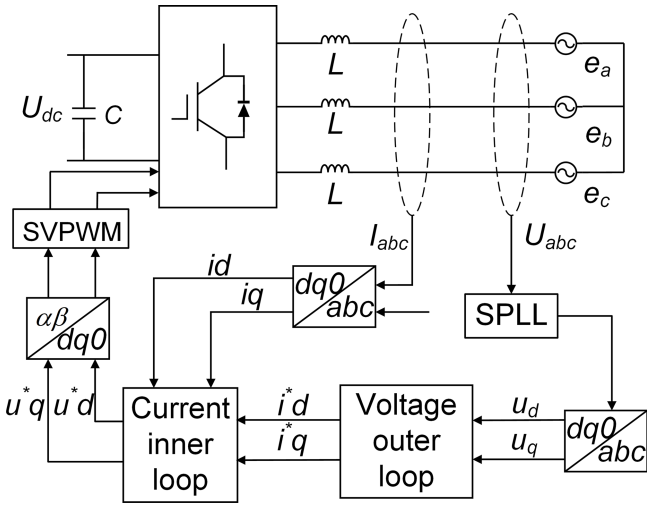

Figure 9: Photovoltaic system converter control block diagram

The mathematical model of the $d-q$ coordinate system (12) reveals a coupling relationship between the d-axis and the q-axis. To attain independent control of the coupling variable separation, the existing inner loop control approach utilizing feedforward decoupling is implemented. The autonomous and precise regulation of the direct currents i_d and i_q is achieved, and components that can mitigate the coupling effects are incorporated. The equation is as follows:

$$\begin{cases} u_d = -\left(K_{iP} + \dfrac{K_{iI}}{s}\right)\left(i^*{}_d - i_d\right) + \omega L i_q + e_d \\ u_q = -\left(K_{iP} + \dfrac{K_{iI}}{s}\right)\left(i^*{}_q - i_q\right) - \omega L i_d + e_q \end{cases} \tag{22}$$

In Formula (22), K_{iP} is the proportional regulation gain of the current inner loop, while K_{iI} represents the integral regulation gain; $i^*{}_d$ is the d-axis current reference value, and $i^*{}_q$ is the q-axis current reference value; $\omega L i_d$ and $\omega L i_q$ are coupling variables.

The feed-forward decoupling model of three-phase voltage source PWM converter in $d-q$ coordinate system can be derived by integrating Eq. (22) with Eq. (12):

$$\begin{cases} L\dfrac{di_d}{dt} = \left(K_{iP} + \dfrac{K_{iI}}{s}\right)\left(i^*_d - i_d\right) \\ L\dfrac{di_q}{dt} = \left(K_{iP} + \dfrac{K_{iI}}{s}\right)\left(i^*_q - i_q\right) \end{cases} \tag{23}$$

Eq. (23) demonstrates the elimination of the two coupling quantities in the $d-q$ axis of the current inner loop, hence achieving decoupling control of the current inner loop. Fig. 10 illustrates the control block diagram of the current feedforward decoupling loop. Among them, i^*_d regulates active power, while i^*_q governs reactive power. To achieve a unit power factor in the system, let $i^*_q = 0$.

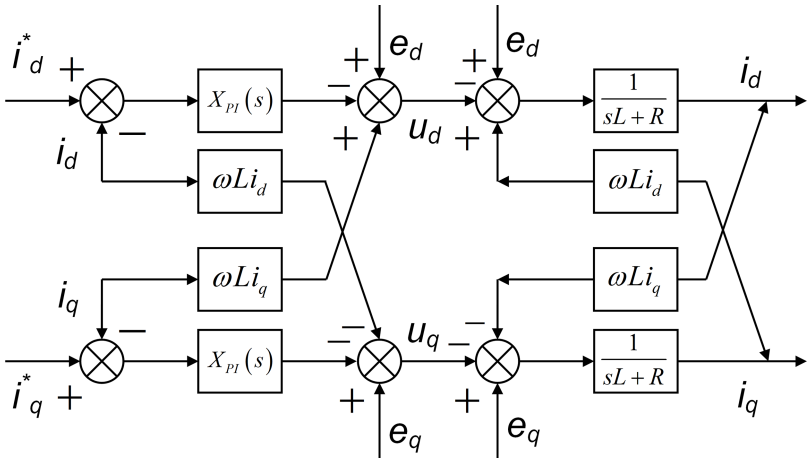

Figure 10: Current feed-forward decoupling loop control block diagram

The prior study indicates that the existing inner loop control can enhance the dynamic reaction speed of the converter and mitigate voltage fluctuations post-decoupling. Fig. 11 illustrates the control procedure of the d-axis current loop after decoupling.

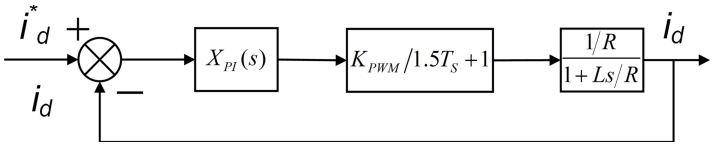

Figure 11: D-axis current loop control process

The image illustrates $X_{PI}(s)$, which denotes the transfer function of the current loop PI regulator; $K_{PWM}/1.5T_s+1$ denotes the pulse width modulation link, where K_{PWM} signifies the converter's equivalent gain, T_s indicates the switching cycle, and $1/1.5T_s+1$ illustrates the delay link, with $1.5T_s$ accounting for the equivalent delay time following PWM generation and dead time; $1/sL+R$ denotes the regulated system. The transfer function of $X_{PI}(s)$ can be derived by analysis:

$$X_{PI}(s) = K_{iP} + \frac{K_{iI}}{s} = K_{iP}\frac{s\tau_i + 1}{s\tau_i} \tag{24}$$

In Eq. (24), K_{iP} denotes the proportional gain of the current loop PI control, while K_{iI} signifies the integral gain of the current loop. $\tau_i = K_{iP}/K_{iI} = L/R$ represents the time constant.

Then the open loop transfer function of the inner loop can be derived:

$$X_{ci}(s) = X_{PI}(s) \cdot \frac{K_{PWM}}{1.5T_s + 1} \cdot \frac{1}{sL + R} \tag{25}$$

To satisfy the requirements of the present inner loop for high current tracking, the current loop is engineered in accordance with the type I system. The specific parameters are shown in Table 1:

Table 1: Type I system dynamic indicators

Parameter name	Parameter value
Damping ratio	$\xi = 0.707$
Overshoot	$\sigma = 4.3\%$
Rise time	$t_r = 4.72\tau$
Phase margin	$\gamma = 65.5$
Cut-off frequency	$\omega_c = 0.455/\tau$

Among the parameters of the type I system, the damping ratio $\xi = 0.707$ is brought in to obtain:

$$\frac{1.5T_s K_{iP} K_{PWM}}{R\tau_i} = \frac{1}{2} \tag{26}$$

The formula for determining the parameters of a PI regulator can be derived concurrently:

$$\begin{cases} K_{iP} = \dfrac{R\tau_i}{3T_s K_{PWM}} \\ K_{iI} = \dfrac{K_{iP}}{\tau_i} = \dfrac{R}{3T_s K_{PWM}} \end{cases} \tag{27}$$

The simplified transfer function of the current loop, as per this design, is:

$$M_{ci}(s) = \frac{1}{1 + 3T_s s} \tag{28}$$

Eq. (28) indicates that the current inner loop, created in accordance with the type I system, can be approximated as an inertial link, with an inertia constant of $3T_s$. The inner current loop exhibits a rapid dynamic reaction when the switching frequency is sufficiently high, and its bandwidth f_{bi} is:

$$f_{bi} = \frac{1}{2\pi(3T_s)} = \frac{1}{6\pi T_s} \approx \frac{1}{20T_s} = \frac{1}{20} f_s \tag{29}$$

In Formula (29): f_s is the current inner loop PWM switching modulation frequency.

Through computational integration, we can obtain: $K_{iP} = 5$, $K_{iI} = 300$.

The voltage outer loop ensures the stability of the output voltage; it mitigates overshoot and fluctuations during load or input voltage variations, hence enhancing the system's resistance to interference. The voltage loop is engineered in accordance with a type II system. The voltage loop control procedure is illustrated in Fig. 12:

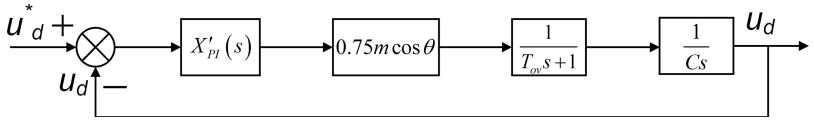

Figure 12: Voltage loop control block diagram

In the diagram, $X'_{PI}(s) = K_{vP} \cdot (T_V s + 1)/T_V s$ denotes the transfer function of the voltage loop PI regulator; K_{vP} signifies the proportional gain of the voltage loop PI control, and K_{vI} indicates the integral gain; T_{ov} denotes inertial properties; $1/Cs$ signifies the integral characteristics of the capacitor. $M_{ci}(s) = 1/1 + 3T_s s$ In contrast to the inner loop, the voltage loop incorporates a time variable $0.75\,m\cos\theta$. To address this issue and prevent complications in the design of the voltage loop, the maximum proportional gain is utilized. Due to $m \le 1$ and $0 \le \cos\theta \le 1$, the maximum value of $0.75\,m\cos\theta$ is 0.75; thus, 0.75 is chosen to substitute the connection. To simplify the structure, the time constant τ_v of the outer loop and the equivalent delay time constant $3T_s$ of the inner loop are summed, that is, $T_{ov} = \tau_v + 3T_s$.

From this, the open loop transfer function of the outer ring can be derived:

$$X_{ov}(s) = \frac{0.75K_v(T_v s + 1)}{CT_v s^2(T_{ov} s + 1)} \tag{30}$$

Voltage outer ring bandwidth:

$$h_v = \frac{T_v}{T_{ov}} \tag{31}$$

According to the integration of type II system design parameters:

$$\frac{0.75K_{vP}}{CT_v} = \frac{h_v + 1}{2h^2{}_v T^2{}_{ov}} \tag{32}$$

Based on the attributes of the voltage outer loop, h_v is frequently assigned a value of 5 in engineering, which is substituted into Eq. (31) to provide $\tau_v = 5T_{ov}$, subsequently leading to the derivation of the PI regulator parameter solution formula:

$$\begin{cases} K_{vP} = \dfrac{4C}{5(\tau_v + 3T_s)} \\ K_{vI} = \dfrac{K_{vP}}{\tau_v} = \dfrac{4C}{25(\tau_v + 3T_s)^2} \end{cases} \tag{33}$$

In the design of the voltage loop utilizing a conventional type II system, the cut-off frequency ω_c is:

$$\omega_c = \frac{1}{2}\left(\frac{1}{T_v} + \frac{1}{T_{ov}}\right) \tag{34}$$

When $\tau_v = T_s$:

$$T_v = h_v T_{ov} = 5(\tau_v + 3T_s) = 20T_s \tag{35}$$

The frequency bandwidth f_{bv} of the voltage outer loop control system is:

$$f_{bv} \approx \frac{\omega_c}{2\pi} = \frac{3}{20T_s \times 2\pi} \approx 0.024 f_s \tag{36}$$

Through computational integration, we can obtain: $K_{vP} = 2$, $K_{vI} = 50$.

4.2 Control Strategy of Voltage Source PWM Converter for Energy Storage System

4.2.1 Grid-Connected Operation Mode

The energy storage system employs PQ control in grid-connected mode, comprising a phase-locked loop module, a coordinate transformation module, a power control loop, and a current control loop as its primary components. The power outer loop primarily oversees and dynamically modifies the output power in real time to attain zero-error control, thereby integrating into the grid with a stable power of 10,000 W. As seen in Fig. 13:

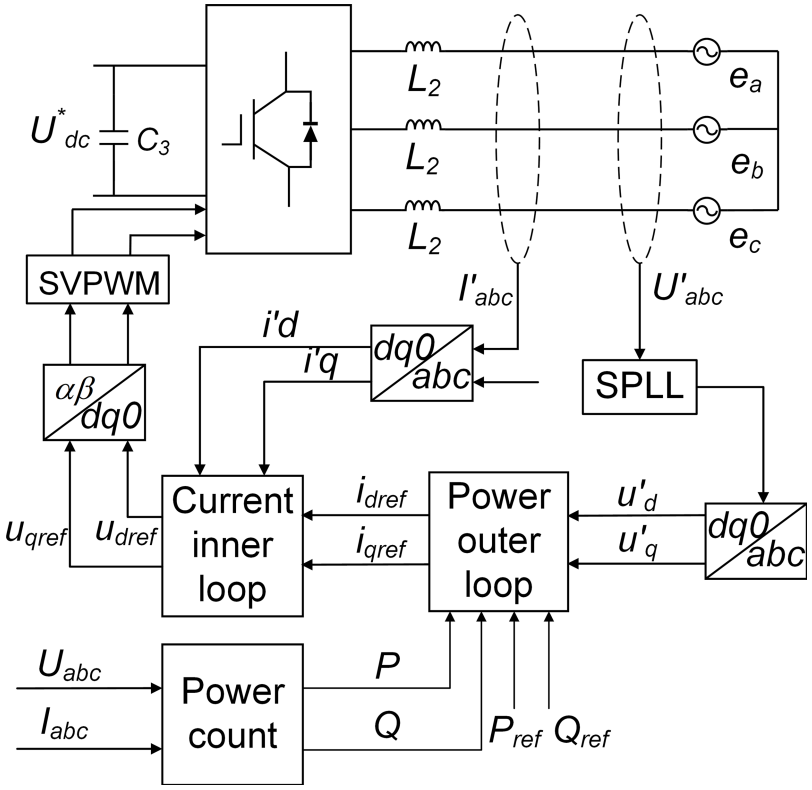

Figure 13: Grid-connected control block diagram of energy storage system converter

The energy storage system is similarly regulated by the PI controller, akin to the solar system, as detailed below:

$$\begin{cases} i_{dref} = \dfrac{2}{3u'_d}\left(K_{pP} + \dfrac{K_{pI}}{s}\right)\left(P_{ref} - P\right) \\ i_{qref} = \dfrac{2}{3u'_q}\left(K_{pP} + \dfrac{K_{pI}}{s}\right)\left(Q_{ref} - Q\right) \end{cases} \tag{37}$$

In Formula (37): i_{dref} denotes the d-axis current reference value in the energy storage system, whereas i_{qref} signifies the q-axis reference value; K_{pP} represents the proportional adjustment gain of the power outer loop, and K_{pI} indicates the integral adjustment gain; P_{ref} denotes the active power setting value, while Q_{ref} signifies the reactive power setting value; P denotes the actual value of the active power of the photovoltaic system, while Q represents the actual value of the reactive power; To achieve a unit power factor, i_{qref} is set to 0, and the control block diagram, which is based on the power outer loop and current inner loop, is illustrated in Fig. 14.

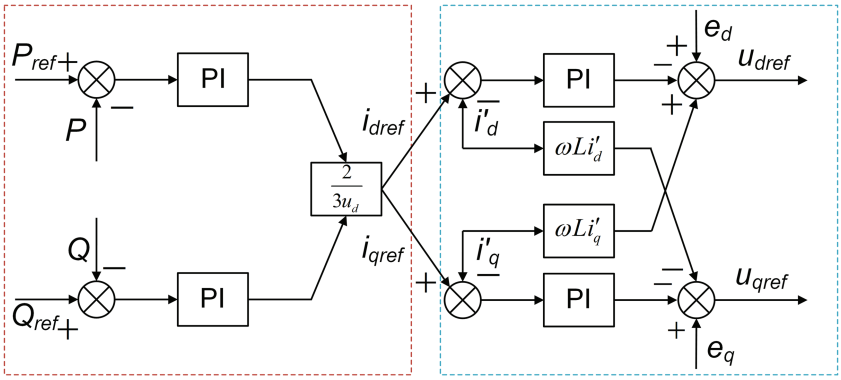

Figure 14: Control block diagram based on power outer loop and current inner loop

The energy storage system's power outer loop control principle parallels the voltage outer loop control principle of the photovoltaic system, while the current inner loop control principle aligns with that of the photovoltaic system; thus, this aspect will not be examined in detail here. By analyzing the integration solution, the proportional gain $K_{iP} = 10$ and the integral gain $K_{iI} = 1000$ of the current loop PI regulation can be obtained. The proportional gain $K_{pP} = 0.01$ and the integral gain $K_{pI} = 0.5$ of the power loop PI adjustment.

4.2.2 Off-Grid Mode

The energy storage system operating in off-grid mode is regulated by VSG, primarily consisting of an active power-frequency loop, a reactive power-voltage loop, and a dual closed-loop control for voltage and current. Currently, energy storage is employed as the main power supply to maintain the voltage and frequency stability of the microgrid and support the microgrid to run stably in the off-grid mode. As illustrated on Fig. 15:

VSG control aims to attain stable regulation of the power grid by emulating the operational characteristics of classic synchronous generators using converters from renewable energy generation equipment, facilitated by algorithms and power electronic control technology. The conventional synchronous generator depends on the mechanical inertia of the rotor and the damping winding to uphold system frequency and voltage stability. The VSG emulates the characteristics of rotor motion equations and excitation regulation via a mathematical model, thereby simulating inertia J and damping D. Formula (38) represents the equation governing rotor motion:

$$\begin{cases} \dfrac{d\delta}{dt} = \omega - \omega_0 \\ J\dfrac{d\omega}{dt} = T_m - T_e - D\Delta\omega = \dfrac{P_m}{\omega} - \dfrac{P_e}{\omega} - D\left(\omega - \omega_0\right) \end{cases} \tag{38}$$

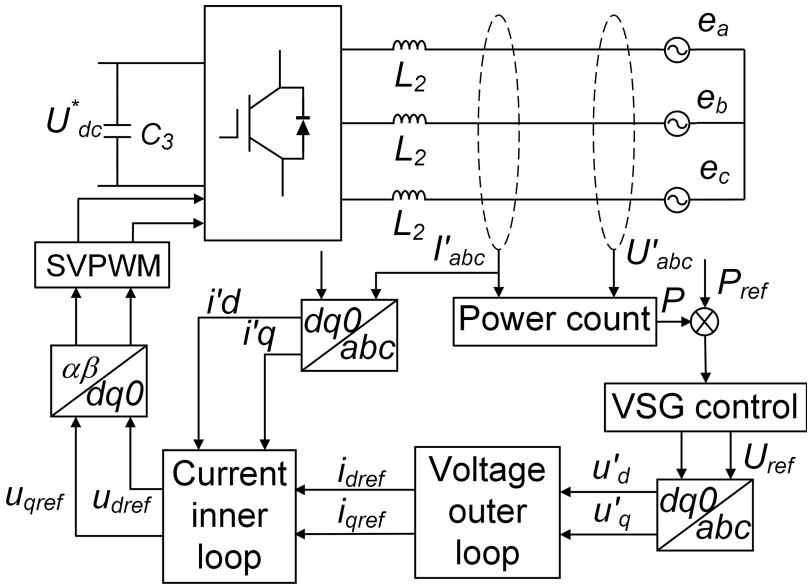

Figure 15: Off-grid control block diagram of energy storage system converter

In Formula (38): δ is the virtual power angle, which represents the phase difference of the system; ω is the virtual rotor angular frequency; ω_0 is the rated angular frequency; T_m and T_e are mechanical, electromagnetic and torque respectively; J is the virtual moment of inertia; D is the virtual damping coefficient; P_m is the mechanical (active) power amplitude; P_e is the electromagnetic power amplitude (the actual output value of active power).

The block diagram of the active-frequency loop control model of the VSG is generated from the second-order model of the traditional synchronous generator, in conjunction with Formula (38), as seen in Fig. 16.

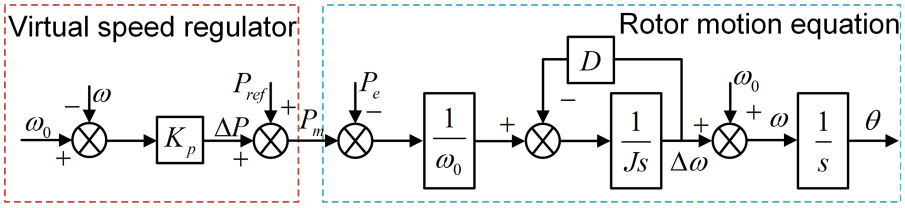

Figure 16: VSG active-frequency loop control block diagram

The primary objective of the excitation control system in a synchronous generator is to uphold the stability of the generator's terminal voltage and to allocate the excitation-induced electromotive force across parallel operating units by modulating the excitation current. This concept is further developed in the VSG control technique. The simulation is executed by the droop characteristics of reactive power-voltage. The relationship between reactive power-voltage control is typically represented by the following equation:

$$U_m = U_0 + k_q\left(Q_{ref} - Q\right) \tag{39}$$

In Formula (39): U_m denotes the reference voltage output value; U_0 signifies the rated voltage; Q_{ref} indicates the reactive power reference value; Q represents the actual reactive power output; k_q is the reactive power-voltage droop coefficient.

The phase reference value is derived from the output voltage amplitude reference of the reactive power-voltage control block diagram in Fig. 17. The integration demonstrates that the VSG reference voltage is represented in Eq. (40):

$$\begin{cases} u_{refa} = E\sin\theta \\ u_{refb} = E\sin(\theta - 2\pi/3) \\ u_{refc} = E\sin(\theta + 2\pi/3) \end{cases} \tag{40}$$

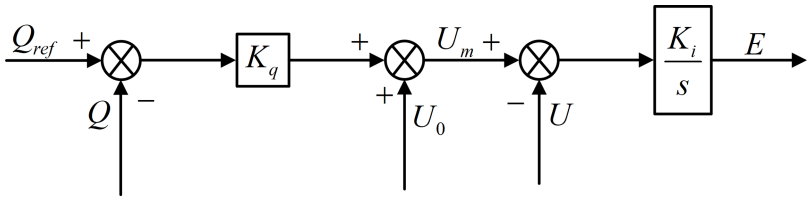

Figure 17: VSG reactive power-voltage loop control block diagram

The structural diagram of the VSG control technique is illustrated in Fig. 18:

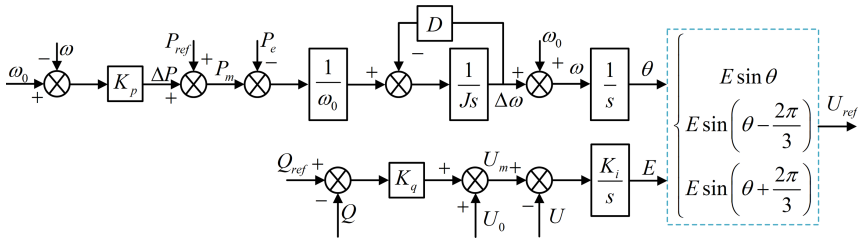

Figure 18: VSG control structure block diagram

In VSG control, the converter's output voltage and current are regulated using dual-loop control, enhancing steady-state precision, current response velocity, and system quality. Moreover, while the essential principles of the double closed-loop control in PWM converters within photovoltaic systems are analogous, there exist distinctions in their primary purposes. In VSG control, it is essential to manage bidirectional energy flow and support the power grid. The d-axis control block diagram is illustrated in Fig. 19:

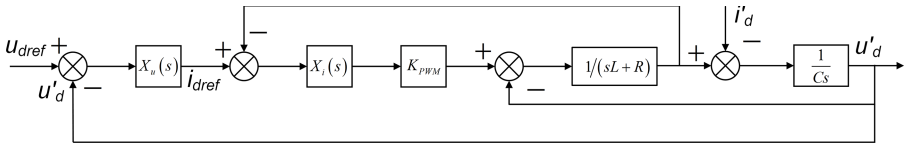

Figure 19: Double-loop control block diagram of d-axis voltage and current

$X_u(s)$ is the voltage loop PI regulation transfer function; $X_i(s)$ is the transfer function of the current loop regulator; K_{PWM} is the converter gain.

4.3 Design and Research of Bidirectional DC/DC Converter in Energy Storage System

To guarantee the reliable functioning of the optical storage microgrid system, it is essential to investigate the control strategy of the bidirectional DC/DC converter. The converter employs a constant current and constant voltage charging mechanism, in conjunction with the lifespan of the energy storage battery. The actual voltage value U^*, computed by calculations, is modified by the PI controller following the discrepancy

between the actual voltage value U^* and the anticipated voltage value U^*_{dc}. Following the restriction of the output current reference value i^*_{bat}, the discrepancy between the actual measured current and the reference value is regulated by the PI controller. Upon constraining and contrasting with the triangle carrier wave, the PWM generator is activated, producing the driving signal for the final output power switch, hence achieving constant current and constant voltage charging. The control block diagram is illustrated in Fig. 20:

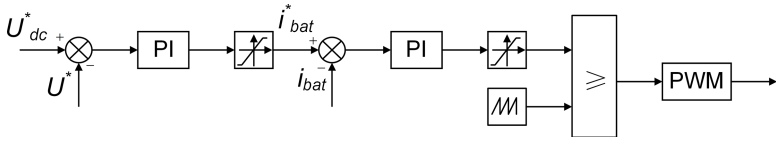

Figure 20: Constant current constant voltage charge control block diagram

During discharge, the converter employs constant current discharge control, utilizing just current loop control. The present output reference value i^*_{bat} diverges from the real current value, which is modified by the PI regulator, then constrained by amplitude, compared to the triangle carrier wave, output from the PWM generator, and ultimately the signal for the output switch tube. Fig. 21 illustrates the control block diagram:

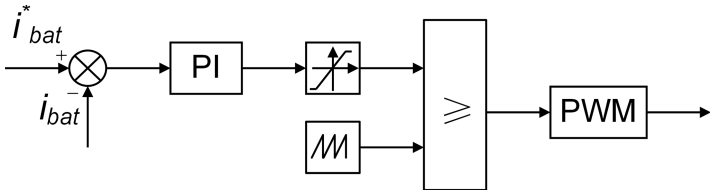

Figure 21: Constant current discharge control block diagram

5 Simulation Analysis

To assess the viability of MPPT control utilizing the particle swarm optimization algorithm, as well as the grid-connected PQ control and off-grid VSG control of the photovoltaic energy storage system proposed herein, a simulation model for both grid-connected and off-grid configurations of the photovoltaic energy storage system is developed in MATLAB/Simulink, as illustrated in Fig. 22.

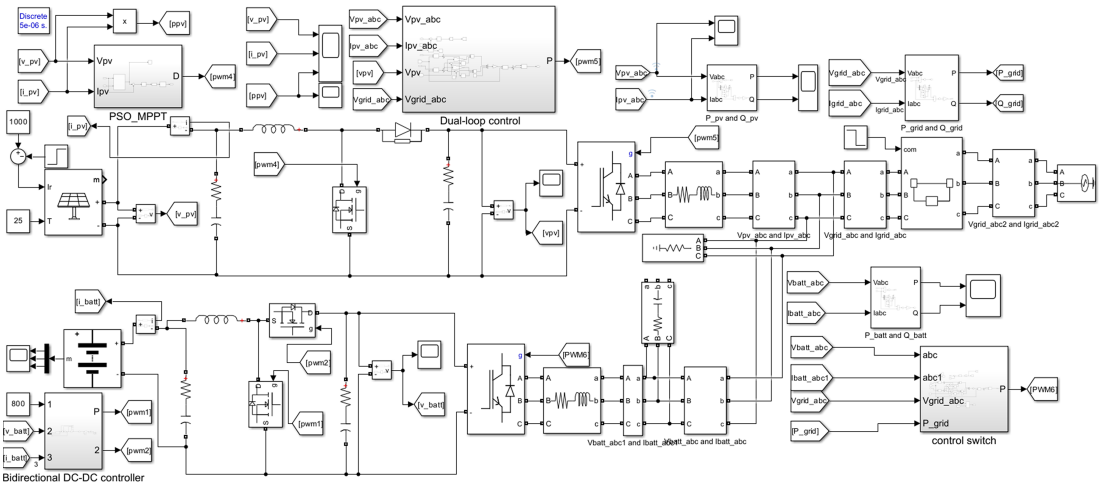

Figure 22: Photovoltaic energy storage system off-grid simulation model

5.1 MPPT Simulation Analysis Based on Particle Swarm Optimization Algorithm

In this paper, the type of photovoltaic panel is ISoltech ISTH-215-P, in which the number of parallel connections is 5 and the number of series connections is 14. This work employs a step change in irradiance to accurately reflect the instability of light intensity in real life. At a light intensity of 1000 W/m^2, the peak power output of an individual photovoltaic panel is around 213.15 W. The estimate indicates that the current maximum power output of the photovoltaic array is around 14,920.5 W. At a light intensity of 700 W/m^2, the maximum power output of a single solar panel is around 150.788 W. The current maximum output of the photovoltaic array is around 10,555.1 W. Fig. 23 illustrates the output power of the solar panel:

The solar array, serving as the primary power supply, will experience significant power fluctuations due to variations in light intensity, whereas temperature has minimal impact on these fluctuations. Consequently, this research establishes the temperature at 25°C, which remains constant throughout the simulation phase. The initial light intensity is 1000 W/m^2. At 0.3 s, the light intensity decreases abruptly to 700 W/m^2 for the simulation.

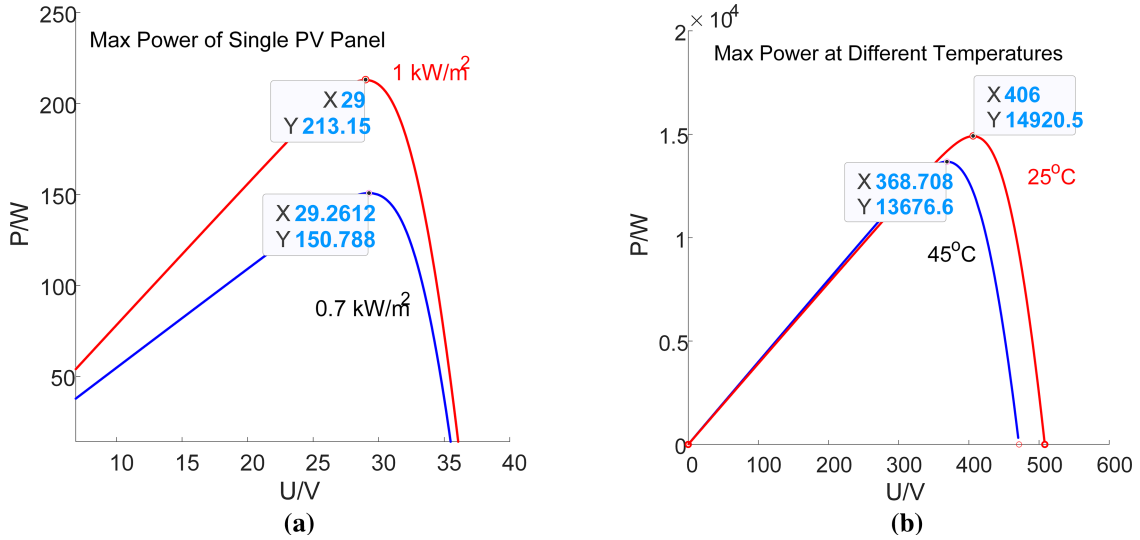

Figure 23: Photovoltaic panel power and voltage diagram. (**a**) Power and voltage of a single photovoltaic panel under different light intensities; (**b**) The power and voltage of photovoltaic array at different temperatures

This research establishes a total simulation duration of 1 s to examine the rapid response capabilities and transient stability of the control system under varying external conditions. Fig. 24 illustrates that at a light intensity of 1000 W/m^2, the particle swarm optimization approach can locate and stabilize the highest power point in around 0.01 s, but the conductance increment method requires about 0.08 s to achieve the same result. Furthermore, the conductance increment approach exhibits significant oscillation between 0 and 0.08 s, accompanied by an overshoot phenomenon, whereas the particle swarm optimization methodology demonstrates minimal oscillation. At 0.3 s, when the light intensity decreases to 700 W/m^2, the particle swarm optimization algorithm can identify and stabilize the maximum power point by 0.31 s without oscillation. In contrast, the conductance increment method tracks the maximum power and stabilizes it only by 0.43 s, exhibiting significant oscillation between 0.3 and 0.43 s. Furthermore, between 0 and 0.3 s, the maximum power point attained by both algorithms after stabilization is approximately the theoretical value of 14,920.5 W. After 0.3 s following the step, upon stabilization, the particle swarm algorithm is closer to the theoretical value of 10,555.1 W, whereas the incremental conductance method deviates significantly. The simulation confirms the efficacy of the particle swarm optimization approach,

demonstrating superior tracking speed and stability compared to the conductance increment method. In varying light intensity conditions, the highest power point identified by the particle swarm optimization technique during simulation is more aligned with the theoretical calculation value, exhibiting superior accuracy compared to the conductance increment method. Attained the required outcomes.

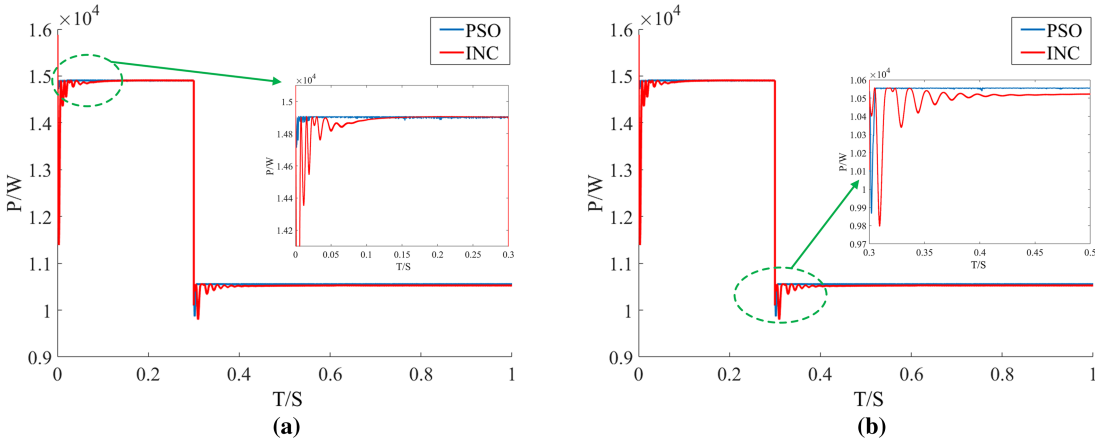

Figure 24: Comparison of particle swarm optimization algorithm and incremental conductance method. (**a**) 0~0.3 s local amplification map; (**b**) 0.3~1 s local amplification map

5.2 Parallel/Off-Grid Simulation Analysis of Photovoltaic Energy Storage System

To thoroughly examine the attributes of the current and voltage in the photovoltaic energy storage system during both grid-connected and off-grid operations depicted in Fig. 22, This work establishes a simulation duration of 1 s, with a constant load consumption power of 4000 W, and delineates the entire operational process into three distinct stages for research and analysis.

During the simulation process, the system temperature is maintained at a constant 25°C, while only the light irradiance is varied to assess the system's response. In the initial phase (0~0.3 s), the light intensity of the photovoltaic array is established at 1000 W/m^2. In the subsequent phase (0.3~0.6 s), the light intensity is reduced to 700 W/m^2 at 0.3 s. In the final phase (0.6~1 s), the photovoltaic energy storage system is deliberately disconnected from the power grid at 0.6 s and transitions to off-grid operation mode. The light intensity of the photovoltaic array currently remains at 700 W/m^2.

This document designates the battery as the energy storage unit. The fundamental specifications are a rated voltage of 400 V, a rated capacity of 200 Ah, and an initial SOC established at 80%. In grid-connected operation, the system delivers an active power of 10 kW and a reactive power of Q = 0 Var, in accordance with the unit power factor needed to satisfy grid connection conditions. There are two prevalent strategies for transitioning from grid-connected to off-grid: planned active off-grid and passive off-grid. This research models and examines the scenario of intended active off-grid systems. The main parameters of the system are as follows: the grid-side filter inductance in the photovoltaic system is 2.1×10^{-2} H, the grid-side filter inductance in the energy storage system is 2.5×10^{-3} H, and the filter capacitance is 2×10^{-5} F.

The voltage and current waveforms on the grid side during the grid-connected period are illustrated in Fig. 25. The operational process exhibits sinusoidal characteristics, while the absence of mutation indicates the system's great stability. Fig. 25a illustrates that the current and voltage attain identical frequency and phase at 0.06 s, indicating a trend towards system stability. Fig. 25b illustrates that at 0.3 s, the output power of the photovoltaic array, prompted by the abrupt change in light intensity, is inferior to that of the power grid, rendering it insufficient for grid connection. The voltage on the grid side remains stable, indicating

that the energy storage battery effectively sustains voltage and current stability during this interval, thereby mitigating system fluctuations resulting from the sudden light variation.

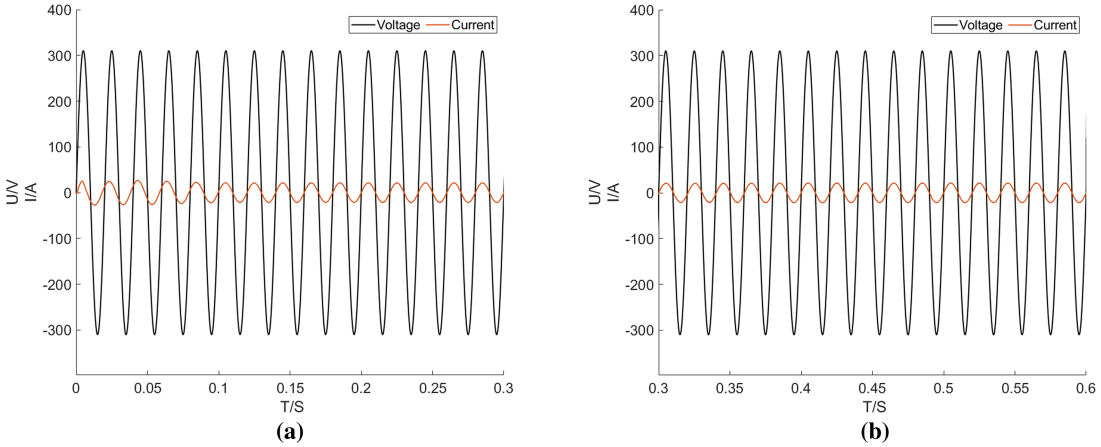

Figure 25: Grid-side voltage and current waveforms. (**a**) 0~0.3 s voltage and current waveforms; (**b**) 0.3~0.6 s voltage and current waveforms

The related power waveforms of the system grid-connected and off-grid are shown in Fig. 26. The research indicates that in the initial phase, the photovoltaic system's output power is approximately 14,920.5 W, with the surplus power remaining after load consumption exceeding the grid's necessary power by 10,000 W. The battery is charged at a power of 920.5 W, and the power value is negative. During the second stage, the residual power output of the photovoltaic system abruptly alters to 6555.1 W, which is inferior to the power grid's output. The battery discharges at 3444.9 W, with a positive power value. In the third step, the system is in an off-grid condition. Currently, after deducing the power necessary for the critical load, the remaining 6555.1 W is being charged to the battery, resulting in a negative power figure. The reactive power of the energy storage system exhibits no overshoot and remains consistently steady at 0 Var.

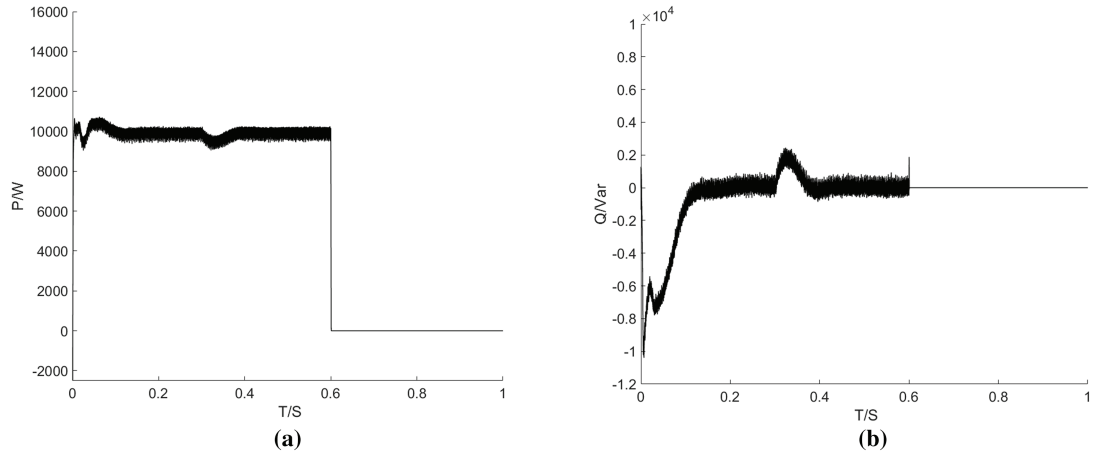

Figure 26: (Continued)

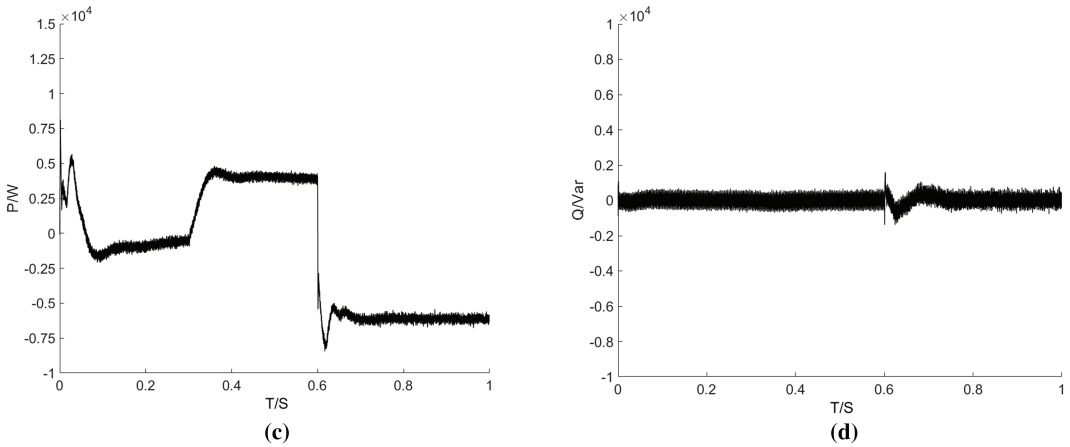

Figure 26: Simulation diagram of grid-connected/off-grid power of photovoltaic energy storage system. (**a**) Power grid active power diagram; (**b**) Reactive power diagram of power grid; (**c**) Active power diagram of energy storage system; (**d**) Reactive power diagram of energy storage system

The charge and discharge state diagram of the battery, as well as the waveform of the voltage and current, are depicted in Fig. 27. The waveform exhibits sinusoidal characteristics, no discernible distortion, and no significant current fluctuations. The figure illustrates that voltage and current stabilization commence at around 0.06 s. Between 0 and 0.3 s, as the battery charges, the SOC increases, resulting in voltage and current oscillating at the same frequency. During battery depletion at 0.3 to 0.6 s, the SOC diminishes, with voltage and current exhibiting identical frequency and phase. When the battery is charged at 0.6 to 1 s, the SOC rises, and the same frequency is reversed.

Fig. 28 illustrates the DC bus output process of solar and energy storage systems. The system promptly monitors the maximum power initially, resulting in transient power and bus voltage overshoots. Both waveforms stabilize approximately at 0.1 s. Upon the reduction of light at 0.3 s, the photovoltaic output power diminishes, leading to a concomitant decline in the DC bus voltage. After 0.6 s, the residual power from the photovoltaic output is utilized to charge the battery, leading to a transient elevation in the bus voltage of the energy storage system, which stabilizes after around 0.05 s. The system's voltage level is progressively stabilized and sustained at 800 V.

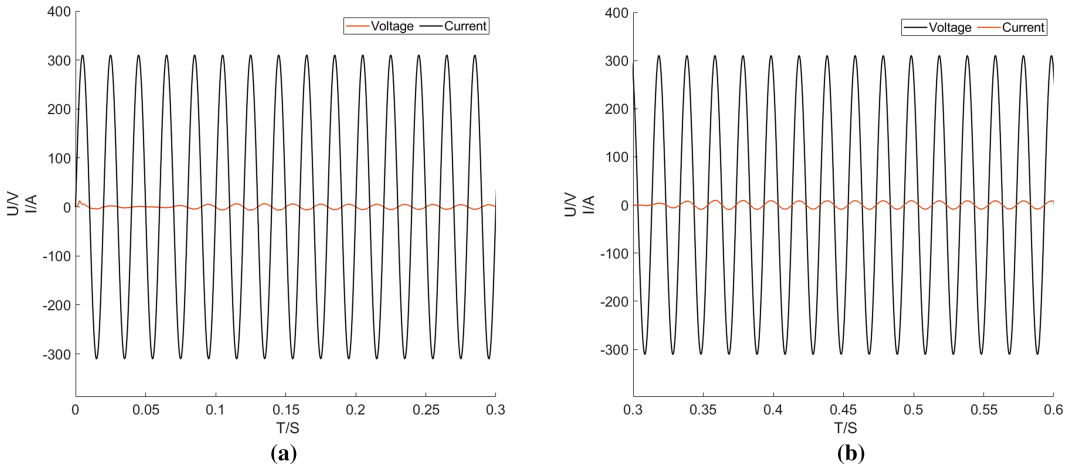

Figure 27: (Continued)

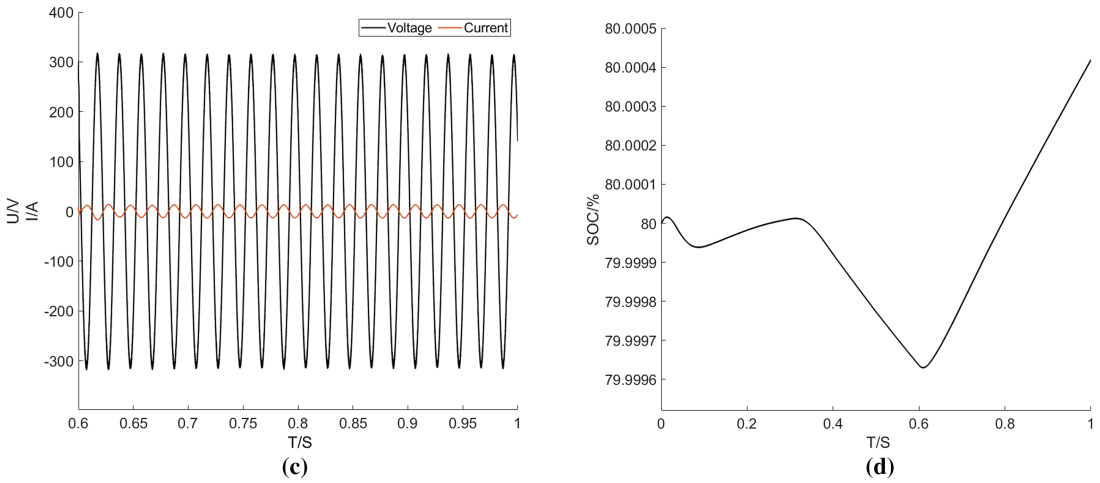

Figure 27: The voltage and current waveforms and the state of charge diagram of the battery side. (**a**) 0~0.3 s voltage and current waveforms; (**b**) 0.3~0.6 s voltage and current waveforms; (**c**) 0.6~1 s voltage and current waveform; (**d**) Charging and discharging state of charge of battery

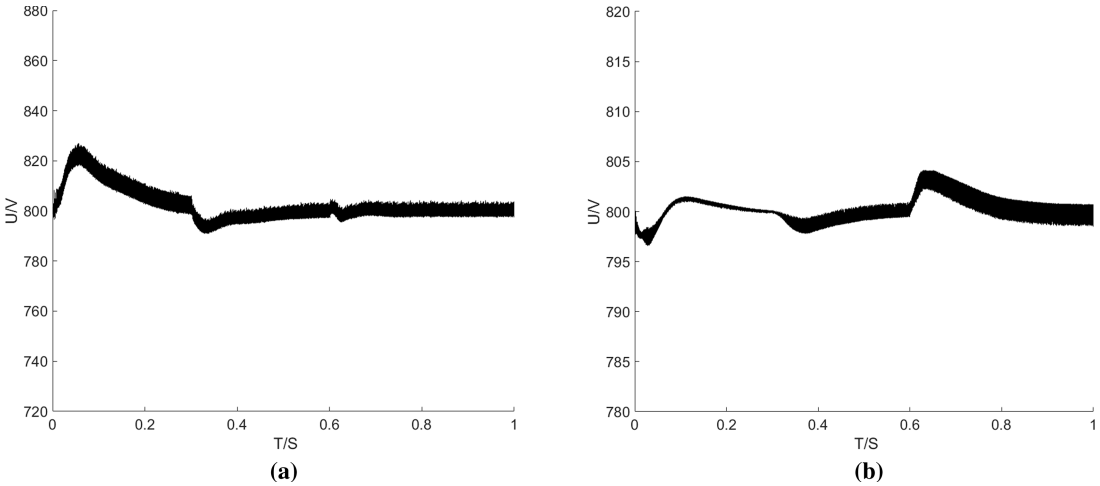

Figure 28: DC bus voltage simulation diagram. (**a**) DC bus voltage diagram of photovoltaic system; (**b**) DC bus voltage diagram of energy storage system

In the context of the photovoltaic energy storage system integrated into the grid, when the system is stable, the total harmonic distortion (THD) of the current, after Fourier transformation, is 3.71%, as illustrated in Fig. 29. This value is below the regulatory threshold of 5%, thereby satisfying the criteria for grid connection.

The examination of Fig. 30a,b indicates that at 0.6 s, the microgrid system transitions to the off-grid state, resulting in fluctuations currently. The frequency fluctuation difference $\Delta \approx 0.09$ Hz produced by the proposed control strategy at 0.6 s is significantly smaller than the fluctuation difference $\Delta \approx 0.2$ Hz generated by the conventional control strategy. Fig. 30c,d illustrates the single-phase current output at the AC bus for both the control strategy and the conventional control method. There is no discernible current overshoot observed upon switching the control strategy. The enhanced control technique demonstrates greater stability and smoothness on the grid side during switching as compared to alternatives.

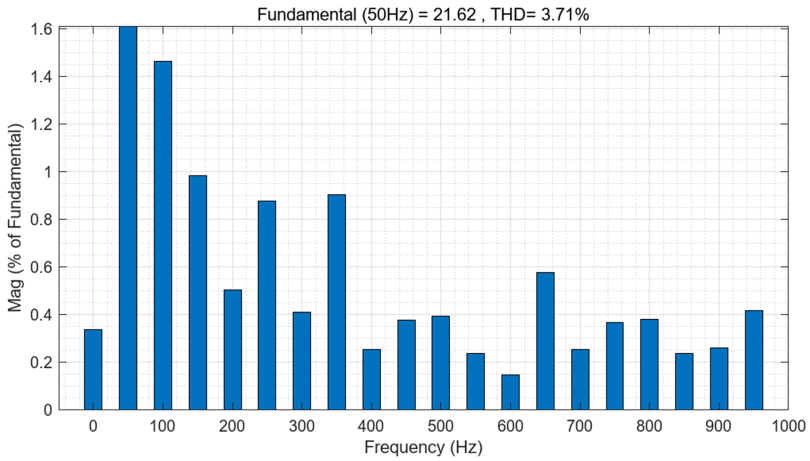

Figure 29: FFT analysis of grid-connected current

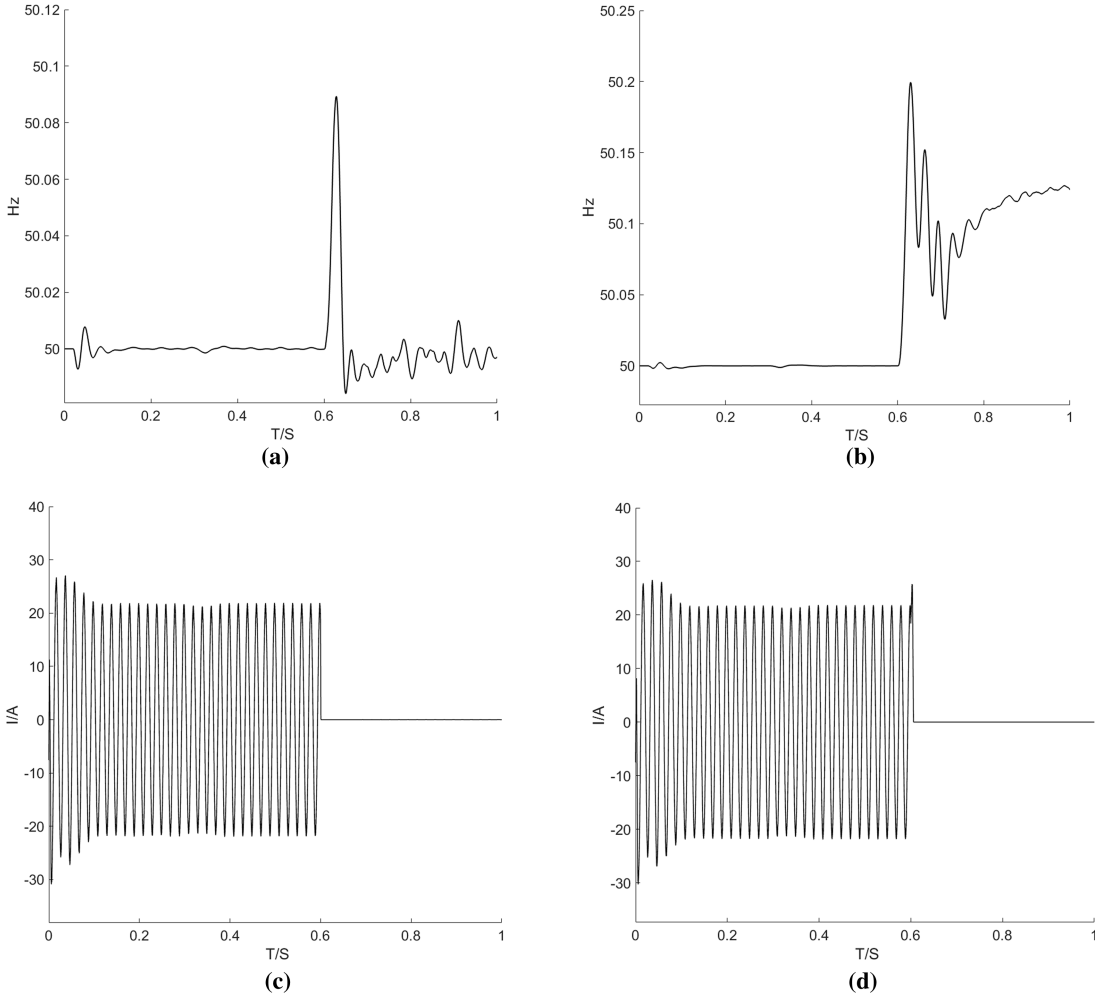

Figure 30: Comparison of frequency and current AC buses under different control strategies. (**a**) Frequency waveform of control strategy in this paper; (**b**) Frequency waveform of conventional control strategy; (**c**) Single-phase current waveform of control strategy in this paper; (**d**) Single-phase current waveform of conventional control strategy

Fig. 31 illustrates the comparative diagram of the current output of the energy storage system: The analysis indicates that the traditional control approach will overshoot upon switching at 0.6 s, but the control strategy presented in this work demonstrates the benefit of a smooth transition.

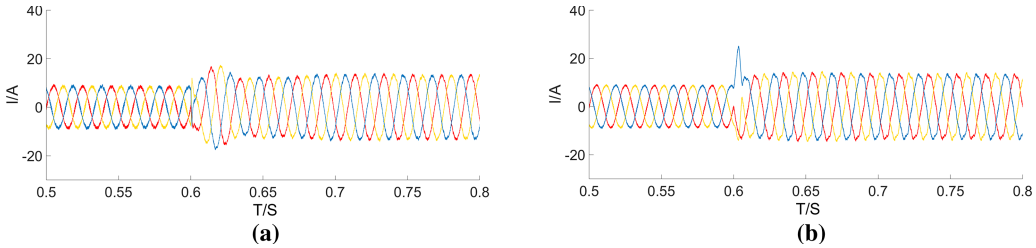

Figure 31: Comparison of current output of energy storage system under different control strategies. (**a**) The current output waveform of the energy storage terminal under the control strategy of this paper; (**b**) The current output waveform of the energy storage terminal under the conventional control strategy

Comparison with Reference [25] and traditional control strategies, as illustrated in Table 2, demonstrates that the control method mitigates the impact of voltage, current, and frequency on the system.

Table 2: The influence of voltage, current and frequency on the system under different control strategies

Attribute	The control strategy of this article	Traditional control strategy	Smooth transition control strategy [25]
U/V	4.2%	5.7%	8.09%
I/A	20%	46.7%	80%
f/Hz	0.09 Hz	0.2 Hz	0.3 Hz

6 Discussion

This paper employs the particle swarm optimization algorithm for maximum power point tracking in photovoltaic systems, excluding the consideration of local shading effects. It analyzes the control strategy transition of photovoltaic energy storage systems from grid-connected to off-grid but does not examine the reverse transition. Furthermore, it verifies only the feasibility of the overall system control strategy, without an in-depth investigation of the power grid's harmonic issues. Considering the constraints of this study and the prospective advancement of photovoltaic energy storage microgrid systems, the course group members intend to engage in comprehensive research and discourse in the subsequent areas:

1. To address the issue of local shading conditions, a refined particle swarm optimization approach is employed to attain more precise maximum power point tracking.
2. The simulation study comparing off-grid and grid-connected systems has been incorporated, and a pre-synchronization control plan module has been introduced to mitigate the transient effects on the system. Attain seamless grid integration.
3. The three-level or multi-level architecture of the three-phase voltage source PWM converter is engineered to diminish grid-connected current harmonics, minimize losses, and enhance conversion efficiency.

7 Conclusions

This work focuses on the maximum power point tracking of solar arrays and the switching between grid-connected and off-grid modes in photovoltaic energy storage microgrids. The contents encompass the MPPT control technique, the three-phase voltage source PWM converter control method, and the bidirectional DC/DC converter. The mathematical modeling, topology, and operational mode of the control strategy are presented. Through theoretical study and simulation validation, the following findings are derived:

1. The suggested MPPT control technique utilizing a particle swarm optimization algorithm attains enhanced response speed, superior tracking precision, and reduced oscillation, hence maximizing the output efficiency of photovoltaic cells.
2. A control technique utilizing feedforward decoupling of the voltage outer loop and current inner loop in a double closed-loop configuration is proposed for a three-phase voltage source PWM converter in solar systems. The converter employs a PQ control approach in the energy storage system when interfaced with the grid. Following the active off-grid phase, the system transitions to a VSG control strategy, with each control strategy operating in conjunction with the others. During the grid-connected phase, it can be integrated into an extensive power system, resulting in stable power output. When the solar cell's power is higher than that of the power grid, the extra energy can be used to charge the energy storage battery and power the grid at the same time. This way, no energy is wasted. When the power is inferior to the power grid, energy storage compensates for the deficit to prevent power fluctuations. Throughout the off-grid duration, energy storage serves as the primary power source to uphold the voltage and frequency stability of the microgrid system. The residual energy from the solar cell utilized by the critical load is still directed into the energy storage battery to compensate for future power deficits or outages.
3. A constant voltage charging and discharging control approach is given for the bidirectional DC/DC converter, which significantly enhances the stability of the DC bus voltage and the charging and discharging efficiency of the energy storage battery.
4. The synchronized implementation of each control technique successfully mitigates power fluctuations. Upon transitioning the grid to off-grid mode, the enhanced control method minimizes transient effects, thereby significantly enhancing power quality and ensuring system stability.

Acknowledgement: Not applicable.

Funding Statement: The authors received no specific funding for this study.

Author Contributions: The authors confirm contribution to the paper as follows: research conception and design: Tao Wang, Ze Feng, Jinghao Ma; data collection: Ze Feng, Jinghao Ma, Shenhui Chen; analysis and interpretation of the results: Jihui Zhang, Tong Wang; manuscript preparation: Ze Feng; vouch: Tao Wang. All authors reviewed the results and approved the final version of the manuscript.

Availability of Data and Materials: The data that support the findings of this study are available from the Corresponding Author, Ze Feng, upon reasonable request.

Ethics Approval: Not applicable.

Conflicts of Interest: The authors declare no conflicts of interest to report regarding the present study.

References

1. Wang T, Ma J, Lin C, Li X, Chen S, Zhang J. Research on the smooth switching control strategy of electric vehicle charging stations based on photovoltaic-storage–charging integration. World Electr Veh J. 2024;15(11):528. doi:10.3390/wevj15110528.
2. Chen L, Xu Q, Yang Y, Gao H, Xiong W. Community integrated energy system trading: a comprehensive review. J Mod Power Syst Clean Energy. 2022;10(6):1445–58. doi:10.35833/mpce.2022.000044.
3. Xiao D. A review on risk-averse bidding strategies for virtual power plants with uncertainties: resources, technologies, and future pathways. Technologies. 2025;13(11):488. doi:10.3390/technologies13110488.
4. Gonzalez-Carreon KM, García Kerdan I. Optimising large-scale solar-based distributed energy generation systems in high-density urban areas: an integrated approach using geospatial and techno-economic modelling. Energy. 2025;327:136425. doi:10.1016/j.energy.2025.136425.
5. Id Ouissaaden F, Dlimi S, Kamel H, Mohssin A, Abdelaziz K. Comparative analysis of P&O and fuzzy logic MPPT techniques for photovoltaic systems under standard and partial shading conditions using DC-DC converters. Int J Eng Res Afr. 2025;75(1):159–73. doi:10.4028/p-n9gkzc.
6. Hasan MG, Uddin MA, Ferdous AHMI, Sadeque MG. Enhanced maximum power point tracking using hybrid GA and PSO algorithms for solar PV systems. Results Eng. 2025;28:107708. doi:10.1016/j.rineng.2025.107708.
7. Zhou R, Xu L, Liu W, Han B, Wan Z. Research on photovoltaic MPPT control algorithm based on improved perturbation and observation methods. Power Supply Technol. 2023;47(3):388–92. (In Chinese).
8. Yaakub MF, Radzi MAM, Noh FHM, Azri M, Shafie S, Azis N, et al. Enhanced incremental conductance MPPT with adjustable reference current and scheduled-gain using a power zoning strategy for flyback-based photovoltaic inverter systems. J Power Energy Eng. 2025;13(9):261–73. doi:10.4236/jpee.2025.139018.
9. Momani RQ, Abuelrub A, Al-Masri HMK, Al-Shetwi AQ. Cost-optimal sizing of battery energy storage systems in microgrids using artificial Rabbits optimization. Energy Nexus. 2025;19:100486. doi:10.1016/j.nexus.2025.100486.
10. Muhammad SA, Jans H, Yusuf PY. Speed improvement of maximum power point tracker (MPPT) based on perturb and observe (P&O) algorithm by using fractional short circuit current (FSCC) on the FPGA. Eng Headw. 2025;27:122–33. doi:10.4028/P-MZXTE1.
11. Xiao Y, Wei H, Wu S, Pan J, Chen T, Zhang H. Research on MPPT control strategy based on LSTM and IHOA algorithm. Electr Power Syst Res. 2026;250:112097. doi:10.1016/j.epsr.2025.112097.
12. Dey B, Jadav R, Kumar RS. Choice of an efficient, sustainable and cost-effective energy storage system for optimal operation of a microgrid system incorporating adaptive demand side management strategies. J Energy Storage. 2025;139:118896. doi:10.1016/j.est.2025.118896.
13. Thi Pham XH. An improved controller for AC/DC hybrid microgrid using bidirectional interlinking converter. J Electr Eng Technol. 2025;2025:1–15. doi:10.1007/s42835-025-02466-1.
14. Alves GH, Guimarães GC, Moura FAM, de Souza AC, Rogério L, Silva LRC. Proposal of a master-slave control for an isolated microgrid after an intentional islanding. J Control Autom Electr Syst. 2023;34(4):731–42. doi:10.1007/s40313-023-01001-9.
15. Wang T, Lin C, Zheng K, Zhao W, Wang X. Research on grid-connected control strategy of photovoltaic (PV) energy storage based on constant power operation. Energies. 2023;16(24):8056. doi:10.3390/en16248056.
16. Vimala D, Vemula NK, Lokeshgupta B, Devarapalli R, Knypiński Ł. Hybrid finite control set model predictive control and universal droop control for enhanced power sharing in inverter-based microgrids. Energies. 2025;18(19):5200. doi:10.3390/en18195200.
17. Zhu Z, Sun S, Ding Y. Research on adaptive smooth switching control strategy for strong and weak power grids in multi-machine parallel PV energy storage VSG system. Glob Energy Interconnect. 2025;8(5):790–803. doi:10.1016/j.gloei.2025.03.005.
18. Liang Z, Mu L, Zhang F, Zhou H, Zhang X. The fault detection method of islanded microgrid with the V/f controlled distributed generation. Int J Electr Power Energy Syst. 2019;112:28–35. doi:10.1016/j.ijepes.2019.04.030.
19. Wang X, Zhang J. Research on an integrated control strategy for grid-connected and off-grid optical storage microgrids. J Phys Conf Ser. 2024;2741(1):012050. doi:10.1088/1742-6596/2741/1/012050.

20. Horrillo-Quintero P, García-Triviño P, Carrasco-González D, Fernández-Ramírez LM. Optimal control strategy based on differential evolution algorithm for seamless transition between islanded and grid-connected operation modes in microgrid clusters. Expert Syst Appl. 2026;297:129461. doi:10.1016/j.eswa.2025.129461.
21. Chen M, Ma S, Wan H, Wu J, Jiang Y. Distributed control strategy for DC microgrids of photovoltaic energy storage systems in off-grid operation. Energies. 2018;11(10):2637. doi:10.3390/en11102637.
22. Mei Y, Zong J. Control strategy of grid-connected inverter based on adaptive virtual synchronous machine. J Power Supply. 2024;45(7):259–66.
23. Liu DB, Li LG, Li SC, Liu GX, Dai X. Coordinated control strategy for isolated DC microgrid with hybrid energy storage system. Renew Energy Resour. 2020;38(4):524–31. (In Chinese). doi:10.13941/j.cnki.21-1469/tk.2020.04.016.
24. Su Z, Shi C, Zhang K, Xie X, Zhang X, Xiao J. TransFCloudNet: a dual-branch feature fusi on ground-based cloud image fine-grained segmentation method for photovoltaic power prediction. Energy Convers Manag. 2026;348:120647. doi:10.1016/j.enconman.2025.120647.
25. Yang Y, Yang K, Shao Y, Chen Y. Research on smooth switching control strategy of microgrid. Renew Energy. 2018;36(1):36–42. (In Chinese). doi:10.13941/j.cnki.21-1469/tk.2018.01.006.